Nanoscale

The Impacts of Dopants on the Small Polaron Carrier Mobility and Conductivity in Hematite - The Role of Disorder

Journal:	*Nanoscale*
Manuscript ID	NR-ART-09-2022-004807.R1
Article Type:	Paper
Date Submitted by the Author:	06-Dec-2022

Complete List of Authors:	Chen, Mingpeng; University of California Santa Cruz, Department of Chemistry and Biochemistry Grieder, Andrew; University of California Santa Cruz, Chemistry and Biochemistry Smart, Tyler; University of California Santa Cruz, Department of Physics Mayford, Kiley; University of California Santa Cruz, Physics Mcnair, Samuel; University of California Santa Cruz, Physics Pinongcos, Anica; University of California Santa Cruz, Chemistry and Biochemistry Eisenberg, Samuel; University of California Santa Cruz, Chemistry and Biochemistry Bridges, Frank; University of California Santa Cruz, Physics Li, Yat; University of California Santa Cruz, Department of Chemistry and Biochemistry Ping, Yuan; University of California Santa Cruz, Chemistry and Biochemistry

The Impacts of Dopants on the Small Polaron Mobility and Conductivity in Hematite - The Role of Disorder

Mingpeng Chen,[†,§] Andrew C. Grieder,[†,§] Tyler J. Smart,[‡,¶] Kiley Mayford,[‡] Samuel McNair,[‡] Anica Pinongcos,[†] Samuel Eisenberg,[†] Frank Bridges,[‡] Yat Li,[†] and Yuan Ping*[,†]

†*Department of Chemistry and Biochemistry, University of California, Santa Cruz, CA, 95064, USA*

‡*Department of Physics, University of California, Santa Cruz, CA, 95064, USA*

¶*Lawrence Livermore National Laboratory, Livermore, California 94551, USA*

§*Contributed equally to this work*

E-mail: yuanping@ucsc.edu

Abstract

Hematite (α-Fe_2O_3) is a promising transition metal oxide for various energy conversion and storage applications due to advantages of low cost, high abundance, and good chemical stability. However, its low carrier mobility and electrical conductivity have hindered wide application of hematite-based devices. Fundamentally, this is mainly caused by the formation of small polarons, which conduct through thermally activated hopping. Atomic doping is one of the most promising approaches to improve the electrical conductivity in hematite. However, its impact on carrier mobility and electrical conductivity of hematite at the atomic level remains to be illusive. In this work, through a kinetic Monte-Carlo sampling approach for diffusion coefficient combined with carrier concentrations computed at the charge neutrality condition, we obtained electrical conductivity of doped hematite. We took contributions from individual Fe-O layers, given that the in-plane carrier transport dominates. We then studied how different dopants impact carrier mobility in hematite using Sn, Ti, and Nb as prototypical examples. We found that the carrier mobility change is closely correlated with the local distortion of Fe-Fe pairs, *i.e.*, the more stretched Fe-Fe pairs are compared to the pristine systems, the lower carrier mobility will be. Therefore, elements which limit distortion of Fe-Fe pair distances from pristine are more desired for higher carrier mobility in hematite. The calculated local structure and pair distribution functions of doped systems have remarkable agreement with experimental EXAFS measurements on hematite nanowires, which further validates our first-principles predictions. Our work revealed how dopants impact carrier mobility and electrical conductivity of hematite, and provided practical guidelines to experimentalists on the choice of dopants for optimal electrical conductivity of hematite and performance of hematite-based devices.

Introduction

Hematite ($\alpha - Fe_2O_3$) is a promising transition metal oxide in energy conversion and storage applications, because of its advantages such as low cost, high abundance, and good chemical stability. Its bandgap around 2.2 eV also makes it an ideal material for visible light absorption; therefore, it is also widely used for photoelectrochemical (PEC) applications. Theoretically hematite's solar-to-hydrogen conversion efficiency could possibly reach 12.9%.[1] However, the experimentally measured efficiency is far below the theoretical value.[2–6] One of the main reasons is its low electrical conductivity due to the formation of small electron polarons (EP).[7] Low EP mobility and concentration lead to low electrical conductivity. Since EP transports through thermally activated hopping, the low mobility is caused by overcoming the energy barrier over 0.1 eV, significantly larger than thermal energy at room temperature k_BT (0.0259 eV). The carrier concentration may be increased by atomic doping as investigated in detail earlier;[8] however, the way polaron mobility is affected by doping remains illusive, despite previous studies.[9–12] Therefore, understanding how atomic doping changes carrier mobility and in turn electrical conductivity is essential and highly desired to boost the performance of hematite-based devices.

Several experimental and theoretical studies have been performed for the effect of atomic doping on the carrier mobility and electrical conductivity of hematite.[9–12] Experimentally, Tian *et al.* synthesized Sn doped hematite and suggested that Sn doping could decrease the energy barrier of EP hopping significantly.[9] However, the referenced pristine hematite hopping barrier (0.52-0.70 eV) is much higher than previously reported experimental and theoretical values (0.11-0.20 eV), and using the latter reference values would lead to the opposite conclusion.[13–17] Past theoretical studies have made significant progress on understanding doping effects on hopping mobility; however, technical challenges remain. For example, Liao *et al.* has studied Ti, Si, Zr, and Ge doping effect on polaron hopping in hematite from first-principles but mainly considered the first EP hop without considering the subsequent EP hoppings with different barriers. This could not provide statistically averaged macroscopic properties for experimental comparison.[10] On the other hand, Kerisit *et al.* employed kinetic Monte-Carlo sampling method for macroscopically-averaged

EP transport properties in doped hematite(Ti, Ca, and Al); however the empirical potential was employed for dopant-polaron and polaron-polaron interactions, where the quantitative accuracy is difficult to evaluate.[11]

Recent works by Zhou *et al.* used ab-initio molecular dynamics to study the *EP* hopping in Si doped hematite which in principles capture more accurately the dopant-polaron interactions at the adiabatic limit. However, macroscopic properties such as carrier mobility and carrier concentrations were not reported. Conclusions are still difficult to draw when comparing with experiments. Besides methodology challenges in past theoretical studies, there is still critical controversy on how atomic doping impacts carrier mobility and electrical conductivity in hematite. As we will show later, our findings agree with Liao *et. al.* and Kerisit *et. al.* on Ti acting as a *EP* trap and decreasing carrier mobility;[10,11] while other works found that certain atomic doping can increase carrier mobility.[9,12]

Herein, to resolve the previous controversy, we carefully evaluated all possible nearest-neighbor *EP* hopping barriers in the supercells from first-principles, followed by using the kinetic Monte-Carlo sampling method for statistically-averaged polaron mobility in doped systems. Multiplied by the carrier concentration, predicted from the method we recently implemented based on charge neutrality condition,[18] the electrical conductivity can be calculated and compared with experimental values. In addition, we studied several different atomic dopants, including both group IV and group V elements, and revealed the trend of how atomic doping impacts the carrier mobility and electrical conductivity in hematite. This knowledge is highly desired because it can provide practical guidelines to experimentalists on the choice of dopants for optimal electrical conductivity and performance of hematite-based devices.

The rest of the paper is organized as follows. First, we calculate the energies of different *EP* configurations locating at different Fe sites. With the Boltzmann distribution, the probability of *EP* forming in each layer is obtained. Second, we compute and compare *EP* hopping mobility of pristine and doped hematite. The *EP* hopping in pristine hematite is studied first as a reference. Dopants of Sn, Ti, and Nb are picked as prototypical examples for detailed discussions of doping

effects. All possible nearest-neighbor *EP* hopping barriers in each layer are computed, used as inputs for kinetic Monte Carlo calculations of in-plane mobility. Then the effective bulk carrier mobility is obtained by summing up in-plane mobility with the probability of *EP* forming at each layer, given the out-of-plane hopping is several orders of magnitude slower than the in-plane one.

The overall electrical conductivity of the whole system can be calculated by multiplying the carrier concentration with the effective bulk carrier mobility, then compared with experimental values. In the end, we use the three dopants to deduce the trend of how different dopants impact carrier mobility and electrical conductivity in hematite. We found that the carrier mobility of hematite decreases after atomic doping regardless of specific elements.

The effect of dopants on carrier mobility is related to the Fe sub-lattice disorder induced by dopants, i.e. the number of distorted Fe-Fe pairs compared to the pristine systems. More distortion introduced to sub-lattice leads to a lower carrier mobility. Therefore, dopants introducing minimal disruption to Fe sub-lattice are more desired for optimal carrier mobility.

Methodologies

First-principles Calculations

We employed the plane-wave density functional theory (DFT) code QUANTUM ESPRESSO[19] for total energy and geometry optimization calculations. We used Perdew-Burke-Ernzerhof (PBE) exchange-correlation functional[20] and an effective Hubbard U value of 4.3 eV[21] for Fe 3d orbitals.[15,16] We used plane-wave cutoffs of 40 Ry and 240 Ry for wavefunction and charge density, respectively, and GBRV ultrasoft pseudopotentials.[22–24] Atomic structures were fully relaxed with an energy threshold of 10^{-4} Ry/Å. We employed a hexagonal $2 \times 2 \times 1$ supercell and a k-point mesh of $2 \times 2 \times 2$ to integrate over the Brillouin zone. We compared the *EP* energy distribution among different Fe sites between $2 \times 2 \times 1$ supercell and $3 \times 3 \times 1$ supercell, and found that the energy difference at the corresponding configuration is less than 0.02 eV (Fig. S6). Considering the high computational cost for calculating $3 \times 3 \times 1$ supercell and relatively small errors between

$2 \times 2 \times 1$ and $3 \times 3 \times 1$ supercells, we employed $2 \times 2 \times 1$ supercell for all other calculations of dopants at the dilute limit. The details of defect formation energy and concentration calculations are consistent with our previous work.[18] The technical detail of carrier mobility methodology by combining the Landau-Zener theory and kinetic Monte-Carlo sampling can be found in Ref. 25.

Doped Hematite Supercell and Kinetic Monte Carlo Sampling

In doped hematite supercells the degeneracy among different Fe sites is broken. To distinguish nonequivalent Fe sites, we labeled different Fe sites on each plane with numbers according to its distance to the dopant (Fig. 1). We also labeled different planes, given that carrier transport mainly happened in plane, and the out-of-plane transport is spin forbidden with orders of magnitude lower mobility.[26] We used the linear interpolation method to calculate the energy barrier of each nearest-neighbor EP hopping, as employed in the previous studies.[15,16] The atom positions are interpolated between the reactant and product configurations, followed by relaxing the approximate saddle-point geometry (the highest energy point in the interpolation pathway). The energy difference between the saddle point and the initial state is 0.11 eV for pristine hematite, consistent with previous literature reports.[15,16] Considering out-of-plane EP hopping is orders of magnitude slower than in the a-b plane,[26] all possible nearest-neighbor in-plane hopping barriers in Sn, Ti, and Nb doped hematite are calculated and listed in Table S1, S2, and S3, respectively. Not all Fe sites can form stable polarons thus hopping barriers involving those sites were not calculated. The mobility was calculated using kinetic Monte Carlo (kMC) sampling.[25] Numerical details of kMC sampling calculations can be found in SI along with its convergence tests.

Electrical Conductivity Ensemble Method

Since doping breaks the atomic-site degeneracy and out-of-plane transport is orders of magnitude lower compared to in-plane, we propose to get an effective carrier mobility (μ_{eff}) in doped

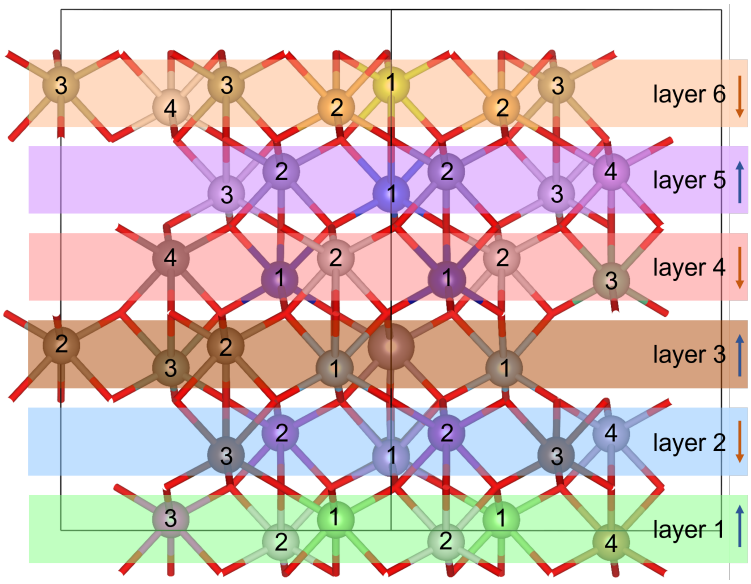

Figure 1. The atomic structure of doped hematite supercell. The balls with numbers denote Fe atoms, the red bar denotes O atoms, and the large gray ball without a number denotes the dopant atom. Dopant subsitutes an Fe site in layer 3, as distinguished by the larger ball in the figure. The supercell is divided into different layers (representing the a-b plane), and for each layer, the Fe sites are labeled with different numbers increasing with their distance to the dopant. The spin direction is also labeled with arrows on the right side of the figure. Spin flips between two nearest planes, which leads to difficulty of out-of-plane polaron transport.

hematite by multiplying the carrier mobility of each layer with the EP formation probability,

$$\mu_{eff} = \sum_{i=1}^{N} p_i \mu_i = \sum_{i=1}^{N} \sum_{j=1}^{M} p_{i,j} \mu_i \tag{1}$$

among which p_i is the probability of EP forming on layer i, $p_{i,j}$ is the probability of forming an EP on site j of layer i, μ_i is the carrier mobility of layer i, and N and M are number of layers and in-plane hopping sites, respectively. The probability distribution ($p_{i,j}$) is computed from energy distribution of EP locating on different sites using Boltzmann distribution. The total probability of EP formation is normalized to one. We adopt different methods to calculate mobility of pristine and doped hematite, given the statistical sampling requirement of the latter, as discussed below. For pristine hematite, the carrier mobility is calculated by using the following equation (giving the

high symmetry of the system):[16]

$$\mu = \frac{ea^2 n\tau_0}{4k_B T} e^{-\frac{E_a}{k_B T}}, \tag{2}$$

where e is electron charge, a is the EP hopping distance, n is the number of equivalent neighbors (which is 3 since we only consider in-plane hopping here), τ_0 is the attempt frequency (168.9 THz^{-1}),[16] and $k_B T$ is thermal energy (0.0259 eV at room temperature). All the values of these parameters can be found in Table S4, and the resulted mobility is listed in Table 1. While for doped hematite, since EP hopping distances and barriers vary at different sites, instead, we use Einstein–Smoluchowski (ES) equation to calculate the mobility,

$$\mu = \frac{eD}{k_B T}. \tag{3}$$

Here D is the diffusion coefficient, obtained from calculating all possible EP hopping in the same layer, with kMC sampling which provides the statistically-averaged value. We note that ES equation is justified in our current condition, i.e. low electric field and room temperature, as discussed in Ref. 27. The effect of dopants on polaron transport depends on the attractive or repulsive interactions between the dopant and polarons, as explained in Ref. 25. Experimentally, previous studies show that low concentration doping or defects still have a non-negligible effect on polaron mobility.[28,29] The computational details can be found in SI. Then the electrical conductivity (σ) in hematite can be calculated by using the following equation,

$$\sigma = en\mu_{eff} \tag{4}$$

where n is the carrier concentration obtained with the method from our previous work.[18]

Results and Discussion

Energy and Associated Probability Distribution of EP Locating on Different Fe Sites

Three prototypical dopants, Sn, Ti and Nb, are selected to study how dopants impact carrier mobility and electrical conductivity of hematite. They are chosen because they are the most well studied group IV and V dopants, with many available experimental results for comparison.[2,5,6,30,31] We have shown the density of states (DOS) and polaron spin density of three dopant systems in SI Fig. S16, where Sn and Ti dopants are at their neutral state, but Nb is at its +1 charged state that leaves only one polaron in the system for fair comparison. We can see the electron polaron state is well localized as a sharp peak in the DOS plot and the polaron spin density appears like a hybridized Fe d-O p orbital. In order to compute the probability of EP formation in each layer, we calculated the formation energy of EP at different Fe sites, shown in Fig. 2(a) and Fig. S7(a) and (c). The EP energy distribution overall follows the trend of Coulomb interaction (i.e. $\sim -1/r$) as a function of dopant-polaron distance (r), where the zero is referenced to the energy of the most stable polaron configuration. Since Sn and Ti (group IV elements) only generate one EP but Nb (group V elements) generates two EPs, for a fair comparison among three dopants, one EP is removed from Nb doped hematite by adding one positive charge. Afterward, the probability of EP forming at different Fe sites is derived from energy distribution based on the Boltzmann distribution, as shown in Fig. 2(b). In addition, the total probability is normalized to one, with the formation probability at each Fe site listed in Table S5. It can be noticed that EP's distribution is dopant-polaron distance dependent and EPs are easier to form on Fe sites closer to the dopant (Fig. 2(b) and S7(b)(d)), consistent with Fig. 2(a).

kMC and Carrier Mobility Calculations

As a reference, EP transport in pristine hematite is studied first, whose carrier mobility is calculated to be 0.056 $cm^2/(V.s)$ as listed in Table 1. The calculated hopping barrier is 0.11 eV (Fig.

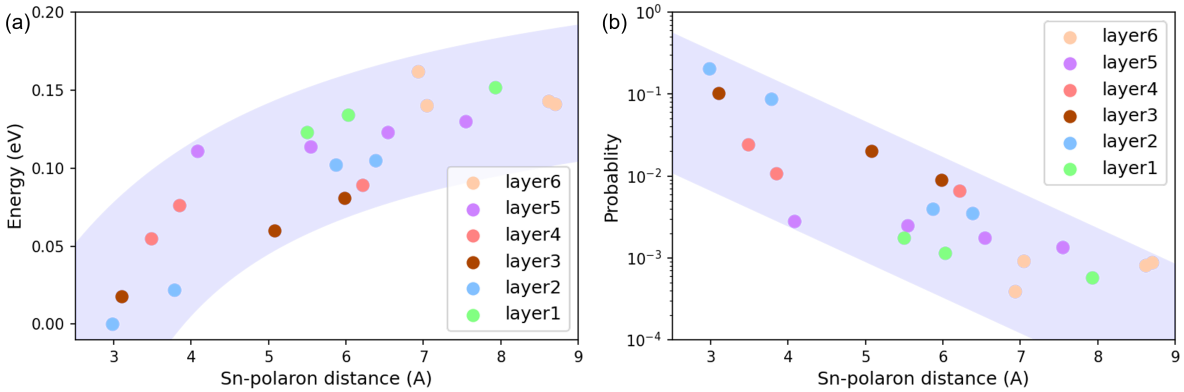

Figure 2. *EP* energy (a) and probability distribution (b) for Sn doped hematite. (a) Energy distribution of *EP* locating at different Fe sites as a function of Sn-polaron distance. The Coulomb interaction trend is highlighted by the wide purple strip. The zero energy is referenced to the energy of the most stable polaron configuration. (b) Probability distribution of *EP* locating at different sites as a function of Sn-polaron distance. A inverse relation between probability and Sn-polaron distance is shown, highlighted in a wide purple stripe. Dopant substitutes the central Fe site in layer 3 as shown in Fig. 1.

S8) in good agreement with experiments.[13] We then study *EP* transport in doped hematite using kMC sampling. All possible nearest-neighbor in-plane *EP* hopping barriers are computed (tabulated in Table S1, S2, and S3), as inputs for kMC diffusion coefficient calculations. The mean square displacement (MSD) is plotted over time in Fig. 3, with its slope corresponding to diffusion coefficient D, and then carrier mobility can be obtained by using Eq. 3. The MSD of pristine system is plotted as a reference with a dashed black line in Fig. 3, and the MSD in each layer of Sn doped system is plotted with colored lines. The latter lines all have a smaller slope than the pristine one, indicating reduced diffusion coefficients at presence of dopants. The carrier mobility of each layer for the three dopants is calculated and listed in Table S5. Afterward, the effective bulk carrier mobility can be calculated by multiplying the probability of *EP* forming at each layer with its corresponding in-plane carrier mobility, i.e. Eq. 1. The effective bulk carrier mobility order for the three dopants is Ti > Sn > Nb, with details in Table 1. Finally, the overall electrical conductivity is obtained by multiplying the carrier concentration with the corresponding system's carrier mobility, which gives good agreement with experimental measured values, as detailed in Table 1.

One note is that our calculated carrier mobility of doped hematite is mostly underestimated compared to the experimental values (less than an order of magnitude). The reason could be the layers far from dopants are difficult to be included completely due to the supercell size limit; however the mobility in these layers is closer to pristine and generally larger than the layers closer to dopants. Specifically, we plot the probability of *EP* formation and carrier mobility over each layer in Fig. S9, where we find a very strong layer dependence for both quantities. Namely, carrier mobility increases with the distance of polarons away from the dopant. An opposite trend is found for the polaron formation probability. The calculated electrical conductivity, on the other hand, has smaller difference between theory and experiments (less than 3 times) and gives the same ordering among dopants between theory and experiments, as shown in Table 1. This illustrates the reliability of our computational method and calculations.

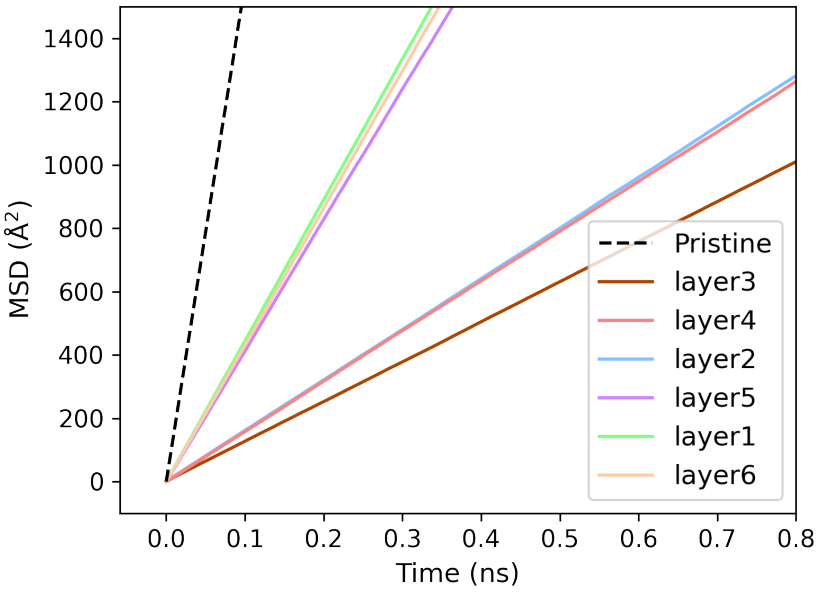

Figure 3. The mean square displacement (MSD) over time for different layers in Sn-doped hematite from the kMC simulations averaging over 16 kMC simulations. Dopant substitutes the central Fe site in layer 3. After the dashed line for pristine, the legend of "layer 3, layer 4..." is in order of increasing distance to the dopant.

Table 1. Comparison between our calculated results and experimental values for carrier concentration (n), effective barrier (E_a), effective carrier mobility (μ), and electrical conductivity (σ). NR represents not reported in past experiments. Pristine carrier concentration is calculated at synthesis temperature of 1073 K and oxygen partial pressure of 1 atm, which is a commonly-used experimental synthesis condition. For doped hematite, 3% doping concentration is achieved by tuning synthesis temperature and oxygen partial pressure, with the computational method in Ref. 18. Then the carrier concentrations and electrical conductivity are calculated under the same condition.

Sample	n (cm^{-3})	E_a (eV)	μ ($cm^2/(Vs)$)	σ (S/cm)
Pristine[Exp, 13]	NR	0.110	NR	NR
Pristine[ours]	1.5×10^{13}	0.110	0.0560	1.34×10^{-7}
Sn 3.0%[Exp, 9]	1.6×10^{19}	0.140	0.0430	0.11
Sn 3.0%[ours]	4.5×10^{19}	0.137-0.185	0.0060	0.04
Ti 3.0%[Exp, 32]	8.8×10^{19}	0.118	0.0405	0.57
Ti 3.0%[ours]	2.7×10^{20}	0.133-0.177	0.0063	0.27
Nb 3.0%[Exp, 31]	5.0×10^{19}	NR	NR	NR
Nb 3.0%[ours]	3.0×10^{20}	0.146-0.219	0.0019	0.09

Effect of Dopant Charge States and Induced Strain

The calculated results above are informative for answering the key questions: how dopants impact the carrier mobility and electrical conductivity in hematite, and what makes a dopant effective in improving carrier mobility and electrical conductivity. To answer these two questions, we started from examining two potentially important factors: one is the charge state of dopants and another is strain induced by atomic doping. In order to study the former, we changed the charge state of dopants by adding positive or negative charges into the supercell calculations. We picked Sn and Nb as examples as follows. For Sn, we simulated neutral (Q0) system (generating one *EP* in the supercell) and negatively-charged (Q-1) system (one negative charge added, two *EP*s in the supercell), in order to compare *EP* hopping barriers between Sn^{4+} and Sn^{3+} doped systems. For Nb, we simulated Q0 system (two *EP*s in the supercell) and Q+1 system (one positive charge added, only one *EP* left in the supercell), to compare *EP* hopping barriers between Nb^{4+} and Nb^{5+} doped systems. We directly calculated and compared energy barriers for the different charged systems mentioned above in Fig. S10. Interestingly, the difference of energy barriers between

differently-charged systems is relatively small, mostly below 0.02 eV. This may indicate that the magnitude of charges in Coulomb interaction among dopant and *EP* may not be a dominant factor for energy barriers.

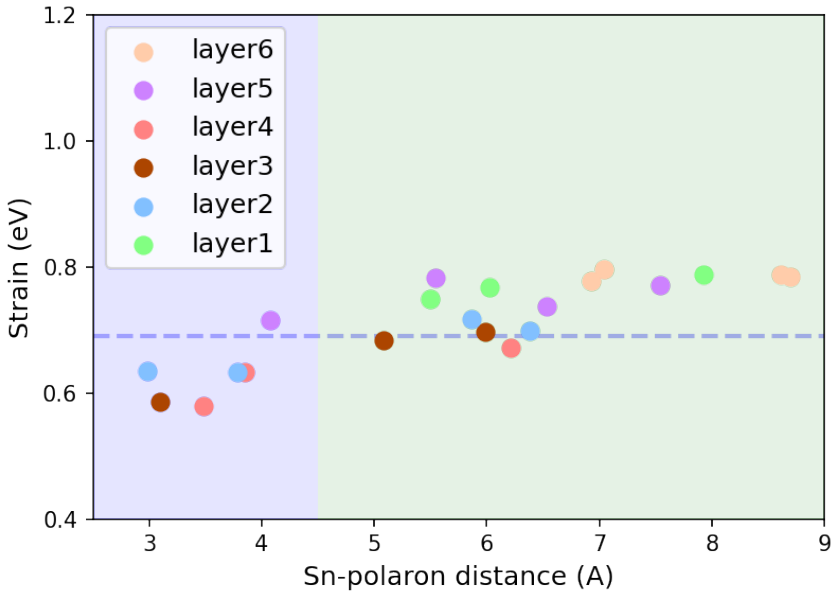

Figure 4. Strain energy of *EP* locating at different Fe sites for Sn-doped hematite as a function of Sn-polaron distance. The dashed horizontal line is the summation of strain energy from isolated Sn dopant and an *EP*. Dopant substitutes the central Fe site in layer 3.

Strain effect was then examined by calculating the strain energy of *EP* locating at different Fe sites, in Fig. 4 for Sn doping and Figs. S11(a), (b) for Ti and Nb doping, respectively. It is computed as the total energy difference of pristine Fe_2O_3 between its equilibrium geometry and the geometry relaxed with dopants (first relax with dopants, then substitute back with Fe atoms to keep the same composition as pristine Fe_2O_3).[8] In Fig. 4, strain energy of all data points can be divided into two regions by taking dopant-polaron distance at 4.5 Å as a threshold (distinguished by different background colors). Beyond this threshold, strain energies are relatively stable and fluctuate within an energy range of 0.1 eV. Therefore, considering that the strain effect is usually local, we propose that there is weaker interaction between the dopant and *EP* when their distance is beyond 4.5 Å. To verify this hypothesis, we calculated the strain energies independently introduced by dopant only and EP only, then summed the two parts up, which is shown as the dashed

horizontal line in Fig. 4 as the non-interacting limit. Specifically, we calculated strain energy of isolated dopant without EP (such as Sn Q+1 system with one positive charge, no polaron left in the supercell), and strain energy due to an isolated *EP* in pristine Fe_2O_3.

It can be noticed that there is some discrepancy between the plateau of calculated strain energy of doped systems with *EP*s and the dashed line (non-interacting limit), which is due to the supercell's finite sizes, as verified by the smaller discrepancy in $3 \times 3 \times 1$ supercell in Fig.S12. When the dopant-polaron distance is short, *i.e.*, below the threshold of 4.5 Å, they are squeezed into a compact space and the strong interaction between them decreases the strain energy to some extent. Similar conclusions can be drawn from other doped systems in Figs. S11(a) and (b). To further understand the strain energy's relation to the hopping barriers, we discuss the local structural distortion induced by different dopants in detail next.

Fe Sub-lattice Distortion and Potential Energy Surface

We then examine the local structure of doped Fe_2O_3. For atomic structural details, we have labeled the Fe-Fe pair distances in pristine and doped Fe_2O_3 (close to dopants) in SI Fig. S17 and Table S6. We then look at Fe-Fe pair distribution function (PDF) averaging over all possible *EP* configurations (where dopant-*EP* distances vary as Fig. 2 and Fig. 4). Fig. 5(a) is the PDF of Fe-Fe pair distances for the three dopants, while Fig. 5(b) is the integrated PDF for the three dopants. The black lines in both panels refer to the values of pristine Fe_2O_3 without distortion as the reference. Comparing with the pristine value, Ti has the smallest Fe-Fe pair distance disorder while Nb has the largest, as indicated by the spread of the peak. We found this trend is consistent with the one of carrier mobility for three dopants (Ti > Sn > Nb). Furthermore, these Fe-Fe pair distances are divided into three regions for more quantitative analysis (Table 2): "Closer" region (Fe-Fe pair distance is shorter than the pristine one by at least 0.01 Å), "Same" region (Fe-Fe pair distance falls within an error bar of ± 0.01 Å compared to the pristine one), and "Farther" region (Fe-Fe pair distance is longer than the pristine one by at least 0.01 Å). Among the three dopants, Nb has the greatest percentage of "Farther" region, which means that it has the most stretched Fe-Fe pair

distances compared to Ti and Sn. In the Fig. 6 schematic plot for polaron hopping in a Marcus-theory-like picture, the scenario (1) shows that a longer Fe-Fe pair distance shifts the potential energy surfaces (PES) of the initial state and the final state horizontally away from each other, which leads to a larger hopping energy barrier. On the other hand, the smallest percentage of "Farther" region in Ti doping suggests the least number of stretched Fe-Fe pair distances. The data in Table 2 is consistent with the calculated carrier mobility trend earlier (Ti > Sn > Nb) in Table 1.

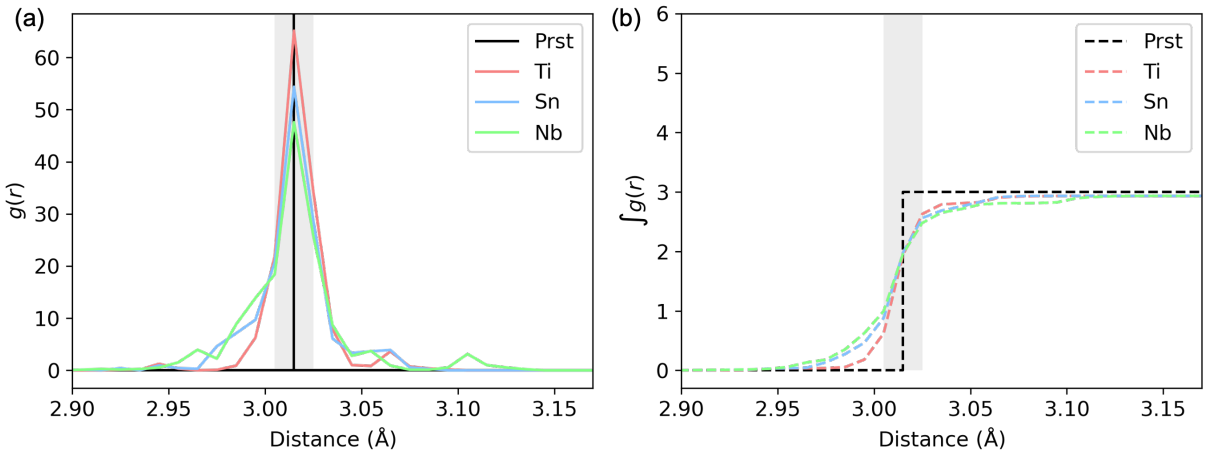

Figure 5. Fe-Fe pair distances for all *EP* configurations for the three dopants. (a) Pair distribution function (PDF) of Fe-Fe pair distances for all *EP* configurations for the three dopants. The black line represents the Fe-Fe pair distance in pristine hematite, used as a reference. (b) Integrated pair distribution function $\int g(r)$ of Fe-Fe pair distance for all *EP* configurations. Grey band indicates region considered as the "Same" region in Table 2. Ti has the least Fe sub-lattice disorder compared to Sn and Nb (closest to the pristine lines).

Table 2. Statistical data for Fe-Fe pair distance falling into three different regions as compared to pristine Fe-Fe pair distance.

Dopant	Closer (%)	Same (%)	Farther (%)
Ti	6.13	88.65	5.22
Sn	15.77	75.45	8.78
Nb	21.26	68.86	9.87

To find a direct correlation between Fe PDF and hopping energy barrier, we plot Fig. 7. In Fig. 7(a), most Fe-Fe pair distance longer than the pristine value exists in supercell configurations

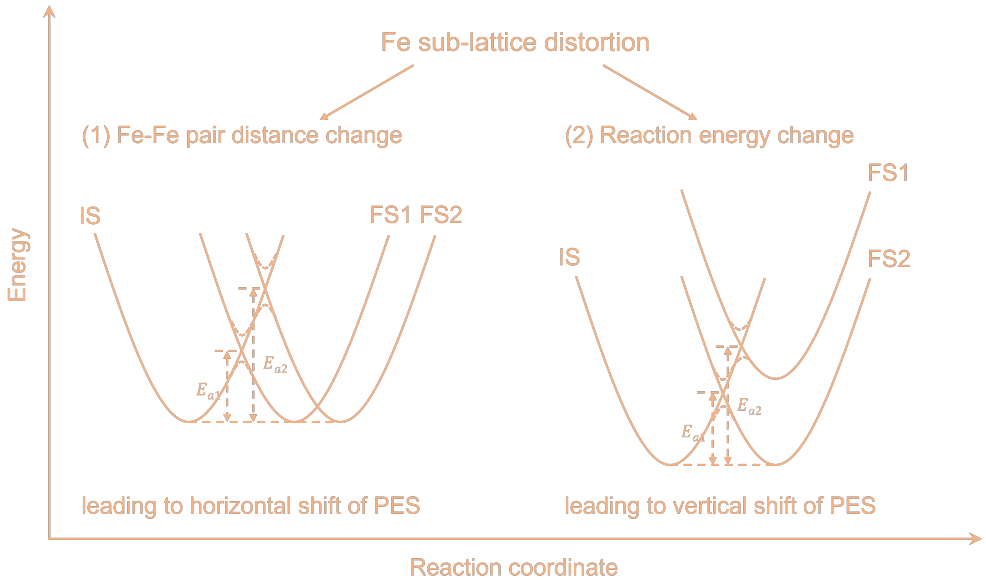

Figure 6. Schematic diagram showing the correlation between Fe-Fe pair distance/reaction energy and energy barrier in a Marcus-theory-like picture. (a) Fe-Fe pair distance change leads to a horizontal shift of potential energy surface (PES). Increasing Fe-Fe distance results in a higher hopping barrier. (b) Reaction energy ($E_{FS} - E_{IS}$) change leads to vertical shift of PES. Increasing final state energy (shifting up its potential energy surface) results in a higher barrier from the initial state (IS) to the final state (FS).

of Sn-polaron distance < 4.5 Å (the blue line). This suggests that the major portion of Fe sub-lattice distortion happens within a threshold of 4.5 Å, correlated well with the Fig. 7(b), where the overall much higher EP hopping barrier exists within the Sn-EP distance < 4.5 Å. This correlation proves that **the Fe sub-lattice distortion is the underlying cause for the change of energy barrier/carrier mobility after doping.** The previous observed layer dependency of carrier mobility can also be explained by the result here. Specifically layers closer to dopants have greater Fe sub-lattice distortion, which results in larger EP hopping barrier, unfavorable for carrier mobility. Additionally, the Fe sub-lattice distortion breaks the potential energy surface (PES) symmetry between initial (IS) and final state (FS) along one hopping path, as illustrated in schematic Fig. 6 scenario (2), which indirectly changes EP hopping barrier. For example, in Fig. S15, considering that the Fe-Fe pair distance is similar between Ti (left panel) and Nb (right panel) doped systems in one particular EP hopping, the much smaller energy barrier in the Ti doped case on the left is due to the vertical down-shift of PES of the FS. This part of contribution is mostly originated from

the reaction energy (E_{FS}-E_{IS}) change as a function of dopant-polaron distance, by an "attractive" or "repulsive" interaction between dopant and *EP*, as discussed in Ref. 25.

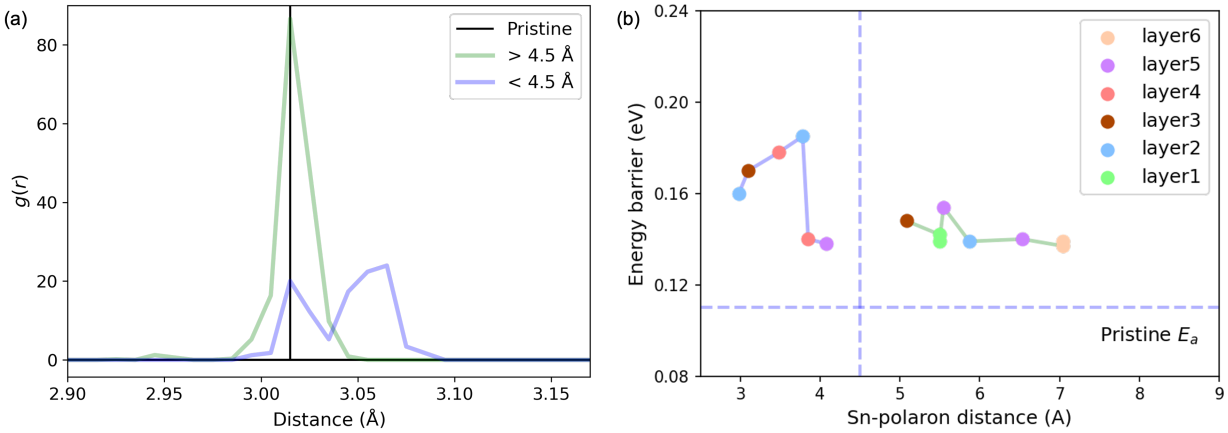

Figure 7. Fe-Fe pair distribution function (PDF) and energy barrier for Sn-doped hematite. (a) PDF of Fe-Fe pair distribution in Sn-doped hematite for Sn-*EP* distance less than 4.5 Å ($<$ 4.5 Å, blue line) or more than 4.5 Å ($>$ 4.5 Å, green line). (b) *EP* hopping barriers in Sn-doped hematite as a function of Sn-*EP* distance. The horizontal dashed line in the plot is the *EP* hopping barrier in pristine hematite. The vertical dashed line is at 4.5 Å to guide the eye.

Experimental Comparison of Local Structure of Doped Fe_2O_3

Since Fe sub-lattice distortion is difficult to be directly compared to experimental data, other relevant parameters are the dopant-O and dopant-Fe distances, which differ from the Fe-O and Fe-Fe distances in pristine hematite. Fortunately, this allows a direct comparison of the calculated pair distances about a dopant atom, with the corresponding measured pair distances from EXAFS. Details of EXAFS measurements and sample synthesis can be found in SI.

The EXAFS results are part of a larger study and are summarized briefly in the SI - See Fig. S4 in SI. The Sn-O, Ti-O, and Nb-O bond lengths for the first oxygen shell, and the Sn-Fe, Ti-Fe, and Nb-Fe pair distances for the first main Fe shell near 3 Å, are extracted from the fits of the EXAFS data and plotted as vertical dashed lines in Fig. 8. In these fits, the first oxygen shells about Ti and Nb remain split into two peaks - as is also the case for the Fe-O peaks in hematite, but for the Sn dopant, the Sn-O peaks move together and can no longer be resolved. (Limit for resolving a split peak is about 0.12 Å for Sn). There is an overall scale factor (by 1.01) difference between

calculations and measured distances, and in Fig. 8 the theoretical distances have been divided by 1.01. The agreement is remarkable - only Sn-O pairs move together in both theory and experiment and the order of the dopant-Fe distances are the same in both theory and experiment.

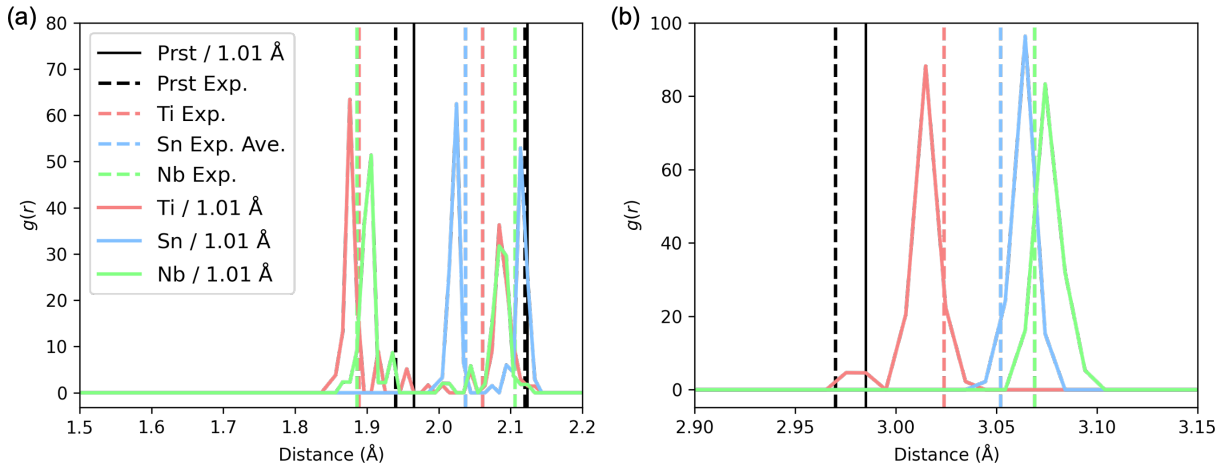

Figure 8. PDF's for all *EP* configurations for the three doped systems. (a) Dopant-O pair distribution function (b) Dopant-Fe pair distribution function. For comparison to experiments, all PDF's are divided by a factor of 1.01. Vertical dashed lines labeled with Exp. are bond lengths fit from EXAFS; see SI for details. For Sn-O the bond lengths of the 2 oxygen neighbors were unresolved and the average was plotted.

Additionally, to further characterize the system we collected X-ray diffraction (XRD) spectra from pristine hematite and 0.1% Sn-doped hematite samples. As shown in Figure S3, the two samples have identical diffraction peaks, which match well with the reported profile for hematite. The results also confirm that there is no observable signal due to impurities. XRD provides the averaged structure which shows the host hematite was not changed by dopants macroscopically.

Conclusion

In conclusion, we systematically investigated how dopants affect carrier mobility and electrical conductivity in hematite. Instead of only focusing on the first *EP* hopping away from the dopant, we studied all possible *EP* hopping in each layer, followed by using kMC sampling for the statistically-averaged carrier mobility. Combined with our previous work on ab-initio carrier

concentration calculation under charge neutrality condition, the overall electrical conductivity is obtained from the product of carrier concentration and carrier mobility. The good agreement between our calculated results and experimental measured values demonstrates the robustness of our computational methods. From our calculated results, we found that doping does not improve carrier mobility in hematite, and the improved electrical conductivity is owing to the enhanced carrier concentration. The Fe sub-lattice distortion is the main underlying reason for the change of carrier mobility. The longer Fe-Fe pair distance is, the larger the hopping barrier is. Among the three dopants studied, Ti shows the highest carrier mobility because Ti has the least Fe sub-lattice distortion (with the lowest percentage of longer Fe-Fe pair distance than pristine). Our work dives deep into understanding how dopants impact the carrier mobility and electrical conductivity of hematite. Additionally, it provides practical guidance to experimentalists about what dopants to choose for optimizing electrical conductivity of hematite and performance of hematite-based devices.

Acknowledgement

This work is supported by the National Science Foundation under grant no. DMR-2003563. Ping acknowledges the financial support from National Science Foundation under grant No. CHE-2203633. Part of this work was performed under the auspices of the U.S. Department of Energy by Lawrence Livermore National Laboratory under Contract DE-AC52-07NA27344. This research used resources of the Scientific Data and Computing center, a component of the Computational Science Initiative, at Brookhaven National Laboratory under Contract No. DE-SC0012704, the lux supercomputer at UC Santa Cruz, funded by NSF MRI grant AST 1828315, the National Energy Research Scientific Computing Center (NERSC) a U.S. Department of Energy Office of Science User Facility operated under Contract No. DE-AC02-05CH11231, the Extreme Science and Engineering Discovery Environment (XSEDE) which is supported by National Science Foundation Grant No. ACI-1548562.[33]

References

(1) Murphy, A.; Barnes, P.; Randeniya, L.; Plumb, I.; Grey, I.; Horne, M.; Glasscock, J. Efficiency of solar water splitting using semiconductor electrodes. *International journal of hydrogen energy* **2006**, *31*, 1999–2017.

(2) Ling, Y.; Wang, G.; Wheeler, D. A.; Zhang, J. Z.; Li, Y. Sn-doped hematite nanostructures for photoelectrochemical water splitting. *Nano letters* **2011**, *11*, 2119–2125.

(3) Wang, G.; Ling, Y.; Wheeler, D. A.; George, K. E.; Horsley, K.; Heske, C.; Zhang, J. Z.; Li, Y. Facile synthesis of highly photoactive α-Fe2O3-based films for water oxidation. *Nano letters* **2011**, *11*, 3503–3509.

(4) Ling, Y.; Wang, G.; Reddy, J.; Wang, C.; Zhang, J. Z.; Li, Y. The influence of oxygen content on the thermal activation of hematite nanowires. *Angewandte Chemie* **2012**, *124*, 4150–4155.

(5) Li, M.; Yang, Y.; Ling, Y.; Qiu, W.; Wang, F.; Liu, T.; Song, Y.; Liu, X.; Fang, P.; Tong, Y., et al. Morphology and doping engineering of Sn-doped hematite nanowire photoanodes. *Nano letters* **2017**, *17*, 2490–2495.

(6) Yang, Y.; Forster, M.; Ling, Y.; Wang, G.; Zhai, T.; Tong, Y.; Cowan, A. J.; Li, Y. Acid treatment enables suppression of electron–hole recombination in hematite for photoelectrochemical water splitting. *Angewandte Chemie International Edition* **2016**, *55*, 3403–3407.

(7) Franchini, C.; Reticcioli, M.; Setvin, M.; Diebold, U. Polarons in materials. *Nature Reviews Materials* **2021**, *6*, 560–586.

(8) Smart, T. J.; Baltazar, V. U.; Chen, M.; Yao, B.; Mayford, K.; Bridges, F.; Li, Y.; Ping, Y. Doping bottleneck in hematite: Multipole clustering by small polarons. *Chemistry of Materials* **2021**, *33*, 4390–4398.

(9) Tian, C. M.; Li, W.-W.; Lin, Y.; Yang, Z.; Wang, L.; Du, Y.; Xiao, H. Y.; Qiao, L.; Zhang, J.-Y.; Chen, L., et al. Electronic structure, optical properties, and photoelectrochemical activity of sn-doped fe2o3 thin films. *The Journal of Physical Chemistry C* **2020**, *124*, 12548–12558.

(10) Liao, P.; Toroker, M. C.; Carter, E. A. Electron transport in pure and doped hematite. *Nano Letters* **2011**, *11*, 1775–1781.

(11) Kerisit, S.; Rosso, K. M. Kinetic Monte Carlo model of charge transport in hematite (α-Fe_2O_3). *The Journal of Chemical Physics* **2007**, *127*, 124706.

(12) Zhou, Z.; Long, R.; Prezhdo, O. V. Why silicon doping accelerates electron polaron diffusion in hematite. *Journal of the American Chemical Society* **2019**, *141*, 20222–20233.

(13) Goodenough, J. B. Metallic oxides. *Progress in Solid State Chemistry* **1971**, *5*, 145–399.

(14) Nakau, T. Electrical conductivity of α-Fe2O3. *Journal of the Physical Society of Japan* **1960**, *15*, 727–727.

(15) Smart, T. J.; Ping, Y. Effect of defects on the small polaron formation and transport properties of hematite from first-principles calculations. *Journal of Physics: Condensed Matter* **2017**, *29*, 394006.

(16) Adelstein, N.; Neaton, J. B.; Asta, M.; De Jonghe, L. C. Density functional theory based calculation of small-polaron mobility in hematite. *Physical Review B* **2014**, *89*, 245115.

(17) Rosso, K. M.; Smith, D. M.; Dupuis, M. An ab initio model of electron transport in hematite (α-Fe 2 O 3) basal planes. *The Journal of Chemical Physics* **2003**, *118*, 6455–6466.

(18) Smart, T. J.; Chen, M.; Grieder, A. C.; Urena Baltazar, V.; Bridges, F.; Li, Y.; Ping, Y. The critical role of synthesis conditions on small polaron carrier concentrations in hematite—A first-principles study. *Journal of Applied Physics* **2021**, *130*, 245705.

(19) Giannozzi, P.; Baroni, S.; Bonini, N.; Calandra, M.; Car, R.; Cavazzoni, C.; Ceresoli, D.; Chiarotti, G. L.; Cococcioni, M.; Dabo, I., et al. QUANTUM ESPRESSO: a modular and

open-source software project for quantum simulations of materials. *Journal of Physics: Condensed Matter* **2009**, *21*, 395502.

(20) Perdew, J. P.; Burke, K.; Wang, Y. Generalized gradient approximation for the exchange-correlation hole of a many-electron system. *Physical Review B* **1996**, *54*, 16533.

(21) Dudarev, S. L.; Botton, G. A.; Savrasov, S. Y.; Humphreys, C.; Sutton, A. P. Electron-energy-loss spectra and the structural stability of nickel oxide: An LSDA+ U study. *Physical Review B* **1998**, *57*, 1505.

(22) Garrity, K. F.; Bennett, J. W.; Rabe, K. M.; Vanderbilt, D. Pseudopotentials for high-throughput DFT calculations. *Computational Materials Science* **2014**, *81*, 446–452.

(23) Kou, T.; Chen, M.; Wu, F.; Smart, T. J.; Wang, S.; Wu, Y.; Zhang, Y.; Li, S.; Lall, S.; Zhang, Z., et al. Carbon doping switching on the hydrogen adsorption activity of NiO for hydrogen evolution reaction. *Nature Communications* **2020**, *11*, 1–10.

(24) Chen, M.; Ping, Y.; Li, Y.; Cheng, T. Insights into the pH-dependent Behavior of N-Doped Carbons for the Oxygen Reduction Reaction by First-Principles Calculations. *The Journal of Physical Chemistry C* **2021**, *125*, 26429–26436.

(25) Wu, F.; Ping, Y. Combining Landau–Zener theory and kinetic Monte Carlo sampling for small polaron mobility of doped $BiVO_4$ from first-principles. *Journal of Materials Chemistry A* **2018**, *6*, 20025–20036.

(26) Iordanova, N.; Dupuis, M.; Rosso, K. M. Charge transport in metal oxides: a theoretical study of hematite α-Fe 2 O 3. *The Journal of Chemical Physics* **2005**, *122*, 144305.

(27) Oberhofer, H.; Reuter, K.; Blumberger, J. Charge Transport in Molecular Materials: An Assessment of Computational Methods. *Chemical Reviews* **2017**, *117*, 10319–10357, PMID: 28644623.

(28) Zhang, W.; Wu, F.; Li, J.; Yan, D.; Tao, J.; Ping, Y.; Liu, M. Unconventional Relation between Charge Transport and Photocurrent via Boosting Small Polaron Hopping for Photoelectrochemical Water Splitting. *ACS Energy Letters* **2018**, *3*, 2232–2239.

(29) Kim, T. W.; Ping, Y.; Galli, G. A.; Choi, K.-S. Simultaneous enhancements in photon absorption and charge transport of bismuth vanadate photoanodes for solar water splitting. *Nature Communications* **2015**, *6*, 8769.

(30) Fu, Z.; Jiang, T.; Liu, Z.; Wang, D.; Wang, L.; Xie, T. Highly photoactive Ti-doped α-Fe_2O_3 nanorod arrays photoanode prepared by a hydrothermal method for photoelectrochemical water splitting. *Electrochimica Acta* **2014**, *129*, 358–363.

(31) Sanchez, C.; Sieber, K.; Somorjai, G. The photoelectrochemistry of niobium doped α-Fe2O3. *Journal of Electroanalytical Chemistry and Interfacial Electrochemistry* **1988**, *252*, 269–290.

(32) Zhao, B.; Kaspar, T.; Droubay, T.; McCloy, J.; Bowden, M.; Shutthanandan, V.; Heald, S.; Chambers, S. Electrical transport properties of Ti-doped Fe_2O_3 (0001) epitaxial films. *Physical Review B* **2011**, *84*, 245325.

(33) Towns, J.; Cockerill, T.; Dahan, M.; Foster, I.; Gaither, K.; Grimshaw, A.; Hazlewood, V.; Lathrop, S.; Lifka, D.; Peterson, G. D.; Roskies, R.; Scott, J. R.; Wilkins-Diehr, N. *Computing in Science and Engineering* **2014**, *16*, 62.